V2487 Oph and 1RXS J173200.0-1934 are closer than the angular resolution of the XMM-Newton instruments (i.e., they are less than ~6 arc sec apart). The ROSAT spectrum (exposure for 462.7 s, with counts in the energy range between 0.75 and 2.4 keV) is compatible with the XMM-Newton spectrum. The 1RXS J173200.0-1934 flux, 3.3×10^{-13} to 8.9×10^{-13} erg cm^{-2} s^{-1}, from the RASS bright source catalog (1RXS-B) is consistent with that from XMM-Newton (9.4×10^{-13} erg cm^{-2} s^{-1}). The similar fluxes indicate that 1RXS J173200.0-1934 and V2487 Oph might be the same object. Therefore, the site of a classical nova may have been seen before the nova explosion itself (as early as 8 years before it), thanks to the x-rays emitted in the accretion flow. This supports the cataclysmic variable scenario for nova explosions.

References and Notes

1. S. Nakano, K. Takamizawa, R. Kushida, Y. Kushida, T. Kato, *Int. Astron. Union Circ. 6941* (1998).
2. A. V. Filippenko *et al.*, *Int. Astron. Union Circ. 6943* (1998).
3. W. Liller, A. Jones, *Inform. Bull. Var. Stars* **4870**, 1 (2000).
4. J. Krautter, H. Ögelman, S. Starrfield, R. Wichmann, E. Pfeffermann, *Astrophys. J.* **456**, 788 (1996).
5. H. Ögelman, M. Orio, J. Krautter, S. Starrfield, *Nature* **361**, 331 (1993).
6. L. Shanley, H. Ögelman, J. Gallagher, M. Orio, J. Krautter, *Astrophys. J.* **438**, L95 (1995).
7. M. Orio, J. Greiner, *Astron. Astrophys.* **344**, L13 (1999).
8. The nuclear burning time scale is defined as the time needed to burn by nuclear reactions (of hydrogen, in novae) all of the remaining envelope. Its value is about 400 years for an envelope mass of $10^{-4} M_\odot$ and a luminosity of $2 \times 10^4 L_\odot$, and it is proportional to mass and inversely proportional to luminosity.
9. R. D. Gehrz, J. W. Truran, R. E. Williams, S. Starrfield, *Pub. Astron. Soc. Pac.* **110**, 3 (1998).
10. M. Orio, J. Covington, H. Ögelman, *Astron. Astrophys.* **373**, 542 (2001).
11. S. N. Shore, S. Starrfield, G. Sonneborn, *Astrophys. J.* **463**, L21 (1996).
12. R. González-Riestra, M. Orio, J. Gallagher, *Astron. Astrophys.* **129**, 23 (1998).
13. K. M. Vanlandingham, G. Schwarz, S. N. Shore, S. Starrfield, *Astron. J.* **121**, 1126 (2001).
14. NASA High Energy Astrophysics Science Archive Research Center (HEASARC) (http://xmm.gsfc.nasa.gov/cgi-bin/Tools/w3nh/w3nh.pl).
15. Parameters of the model best fitting the spectra of V2487 Oph follow, with 1σ uncertainties. Low-T MEKAL: kT (keV) $= 0.22 \pm 0.01$, emission measure $(3.1^{+0.3}_{-0.2}) \times 10^2$ $(d/10$ kpc$)^2 \times 10^{55}$ cm^{-3}; high-T MEKAL: kT (keV) ≥ 48, emission measure 3.5 $(\pm 0.9) \times 10^2$ $(d/10$ kpc$)^2 \times 10^{55}$ cm^{-3}; Gaussian line: E_{line} (keV) $= 6.5 \pm 0.1$, σ_{line} (keV) $= 0.6 \pm 0.1$, F_{line} (photons cm^{-2} s^{-1}) $= (6.6^{+1.3}_{-1.1}) \times 10^{-5}$. Blackbody temperature and absorption N_H have been fixed (30 eV and 4×10^{21} cm^{-1}, respectively). The emission measure of the MEKAL plasma model is defined as $\int n_e n_H dV$ (where n_e and n_H are the electron and hydrogen densities, in cm^{-3}, and V is the volume of the emitting plasma). The bolometric flux of the blackbody component is 2.9 (± 0.7) $\times$ $(d/10$ kpc$)^2 \times 10^{37}$ erg s^{-1}, and the total absorbed flux, in the 0.3 to 8.0 keV range, is 4.6×10^{-12} erg cm^{-2} s^{-1}, yielding an x-ray luminosity of 5.2 $(d/10$ kpc$)^2 \times 10^{34}$ erg s^{-1}. The reduced χ^2 of the fit is $\chi^2_\nu = 1.18$, with number of degrees of freedom $\nu = 340$.
16. The distance to V2487 Oph derived by Lynch *et al.* (*30*) was 27 ± 3 kpc. They used an empirical $M_V^{max}(t_2)$ relation to obtain M_V^{max} (absolute visual magnitude at

maximum), the apparent visual magnitude at maximum m_V^{max} from observations (*1*), and the visual extinction, $A_V = 1.16 \pm 0.24$ mag; they obtained A_V from the color excess E(B-V) $= 0.38 \pm 0.08$ obtained from the observed OI λ8446 and λ11287 near-infrared lines. The distance 27 kpc is very large, and its determination should be taken with caution. It is probable that for very fast novae (such as V2487 Oph), the real visual maximum is missed by observers and therefore the true m_V^{max} is much brighter. The faintness of the nova ($m_V = 9.5$ at discovery) further prevents its discovery at maximum. An estimation of m_V^{max} follows from extrapolation of the visual light curve back in time to the prediscovery data or to some reasonable m_V^{max}, with a slope dictated by t_2 or t_3 (*31*). This exercise yields m_V^{max} in the range 6.8 to 9.5, leading to a distance between 8 and 27 kpc (for $M_V^{max} = -8.8$ and $A_V = 1.16$). Another source of uncertainty is the empirical $M_V^{max}(t_2)$ relation, which should not necessarily be valid for all the systems (although it is generally accepted as such).
17. J. MacDonald, S. Vennes, *Astrophys. J.* **373**, L51 (1991).
18. S. Balman, J. Krautter, H. Ögelman, *Astrophys. J.* **499**, 395 (1998).
19. S. Balman, J. Krautter, *Mon. Not. R. Astron. Soc.* **326**, 1441 (2001).
20. The nova GQ Mus has the longest turnoff time observed to date, 9 years (*5*), and nova LMC 1995 was still emitting soft x-rays in 2000 (*32*). These two novae and V2487 Oph are the only ones to date with observed (through x-rays) turnoff times longer than 3 years.
21. R. Mewe, J. S. Kaastra, D. A. Liedhal, *Legacy* **6**, 16 (1995); available at http://heasarc.gsfc.nasa.gov/docs/journal/meka6.html.
22. K. Arnaud, B. Dorman, *XSPEC User's Guide for Version 11.1.x* (HEASARC, NASA/GSFC, Greenbelt, MD, 2001).
23. J. Patterson, J. C. Raymond, *Astrophys. J.* **292**, 535 (1985).
24. M. Ishida, K. Mukai, J. Osborne, *Publ. Astron. Soc. Jpn.* **46**, L81 (1994).
25. C. Hellier, K. Mukai, M. Ishida, R. Fujimoto, *Mon. Not. R. Astron. Soc.* **280**, 877 (1996).
26. R. Fujimoto, M. Ishida, *Astrophys. J.* **474**, 774 (1997).
27. I. Hachisu, M. Kato, T. Kato, K. Matsumoto, preprint available at http://xxx.lanl.gov/astro-ph/0110265.
28. M. Livio, A. Shankar, J. W. Truran, *Astrophys. J.* **330**, 264 (1988).
29. W. Voges *et al.*, *Astron. Astrophys.* **349**, 389 (1999); available at www.xray.mpe.mpg.de/rosat/survey/rass-bsc.
30. D. K. Lynch, R. J. Rudy, S. Mazuk, R. C. Puetter, *Astrophys. J.* **541**, 791 (2000).
31. M. J. Harris *et al.*, *Astrophys. J.* **522**, 424 (1999).
32. M. Orio, J. Greiner, W. Hartmann, M. Still, in *Classical Nova Explosions*, M. Hernanz and J. José, Eds., AIP Conference Proceedings, vol. 637 (AIP, New York, 2002), pp. 355–359.
33. S. Snowden, M. Still, I. Harrus, P. Brendan, *An Introduction to XMM-Newton Data Analysis* (NASA/GSFC XMM-Newton Guest Observer Facility, Greenbelt, MD, 2001).
34. This work is based on observations obtained with XMM-Newton, a European Space Agency (ESA) science mission with instruments and contributions directly funded by the ESA member states and by NASA. Supported in part by the Ministerio de Ciencia y Tecnología.

Magnetic Superstructure in the Two-Dimensional Quantum Antiferromagnet SrCu$_2$(BO$_3$)$_2$

K. Kodama,[1] M. Takigawa,[1]* M. Horvatić,[2] C. Berthier,[2,3] H. Kageyama,[1] Y. Ueda,[1] S. Miyahara,[1,4] F. Becca,[4] F. Mila[4]

We report the observation of magnetic superstructure in a magnetization plateau state of SrCu$_2$(BO$_3$)$_2$, a frustrated quasi–two-dimensional quantum spin system. The Cu and B nuclear magnetic resonance (NMR) spectra at 35 millikelvin indicate an apparently discontinuous phase transition from uniform magnetization to a modulated superstructure near 27 tesla, above which a magnetization plateau at 1/8 of the full saturation has been observed. Comparison of the Cu NMR spectrum and the theoretical analysis of a Heisenberg spin model demonstrates the crystallization of itinerant triplets in the plateau phase within a large rhomboid unit cell (16 spins per layer) showing oscillations of the spin polarization. Thus, we are now in possession of an interesting model system to study a localization transition of strongly interacting quantum particles.

The competition between itinerancy favored by kinetic energy and localization favored by repulsive interactions is a fundamental aspect of many-body quantum systems, of which the Mott (metal-insulator) transition is an example (*1*). Similar phenomena may occur for the spin degrees of freedom of certain magnetic insulators, known as spin liquids, in which the ground state is a singlet separated from triplet excitations by a finite energy gap Δ. Transition metal oxides exhibiting this kind of physics have been actively studied in an effort to understand the more complex physics of high-temperature superconductors [e.g., (*2*)], a good example being spin ladders (*3*). In such systems, a magnetic field $H_c =$

[1]Institute for Solid State Physics, University of Tokyo, Kashiwa, Chiba 277-8581, Japan. [2]Grenoble High Magnetic Field Laboratory, CNRS and MPI-FKF, 38042 Grenoble, France. [3]Laboratoire de Spectrométrie Physique, Université Joseph Fourier Grenoble I, 38402 St.-Martin d'Hères, France. [4]Institut de Physique Théorique, Université de Lausanne, CH-1015 Lausanne, Switzerland.

*To whom correspondence should be addressed. E-mail: masashi@issp.u-tokyo.ac.jp

$\Delta/g\mu_B$ (where g is the effective g-value of the electron spin and μ_B is the Bohr magneton will close the gap, and the resulting magnetization is a gas of mobile triplets whose density can be tuned by the field value. However, when this density becomes commensurate with the underlying crystal lattice, the triplets may crystallize into a superlattice. The magnetization density will then stay constant for a certain range of magnetic field, resulting in a magnetization plateau (4, 5), which has indeed been observed in some quantum spin systems (6, 7). It was argued theoretically that a magnetization plateau at a fractional value of 1 μ_B per unit cell occurs only when translational symmetry of the crystal lattice is broken by a magnetic superlattice (8). We report direct observation of

such a magnetic superlattice by NMR experiments in $SrCu_2(BO_3)_2$, a quasi–two-dimensional quantum spin system.

The planar network of orthogonal dimers of spin 1/2 Cu^{2+} ions in $SrCu_2(BO_3)_2$ (Fig. 1A) (9) has stimulated extensive experimental (10–16) and theoretical (17–23) work. This compound is a realization of the Shastry-Sutherland model (Fig. 1B) conceived theoretically two decades ago (24):
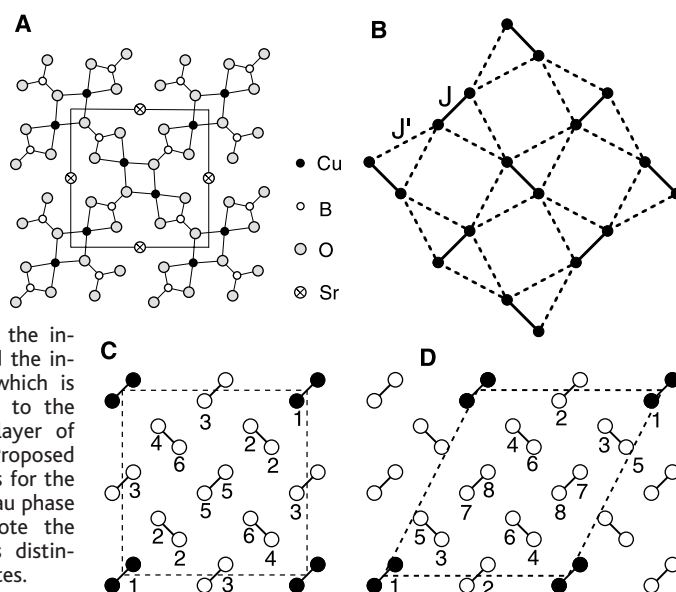
$$H = J\sum_{(n.n.)} \mathbf{S}_i \cdot \mathbf{S}_j + J' \sum_{(n.n.n.)} \mathbf{S}_i \cdot \mathbf{S}_j \quad (1)$$

where J and J' are respectively the nearest neighbor (intradimer) and the next nearest neighbor (interdimer) antiferromagnetic exchange constants between two $S = 1/2$ spins $\mathbf{S}_i$ and $\mathbf{S}_j$. When J is much larger than J', the

model reduces to a collection of dimers. In the opposite limit, $J/J' \ll 1$, it is equivalent to the antiferromagnetic Heisenberg model on a square lattice with a Néel ordered ground state. The Shastry-Sutherland model has the property that the direct product of the dimer singlet states is the exact ground state when J'/J is smaller than a certain critical value near 0.7 (17, 18, 22, 24). An excited state can be made by promoting a singlet dimer into a triplet state, which can then hop from one dimer to another when $J' \neq 0$. The frustration between J and J' in the Shastry-Sutherland model, however, inhibits such hopping up to fifth order of the perturbation series in J'/J, leading to extremely flat triplet bands (i.e., a very small kinetic energy) (18).

Various experiments have established that the dimer singlet ground state (10, 12) is indeed realized in $SrCu_2(BO_3)_2$, with an energy gap to magnetic excitations of 3.0 meV (13, 14). Nearly flat triplet bands were also observed by neutron inelastic scattering experiments (14, 15). The most striking property of $SrCu_2(BO_3)_2$ is the plateaus in the magnetization curve at 1/8, 1/4, and 1/3 of the fully saturated moment (10, 11). One can expect that the small kinetic energy of triplets in the Shastry-Sutherland model will allow them to crystallize into a superlattice at these commensurate densities if there are repulsive interactions between triplets. This is analogous to the Wigner crystallization or charge ordering of electron systems. Although theories have indeed supported such a picture (19–21, 23) and predicted possible structures of the superlattices (19–21), no experimental evidence has yet been reported. Inequivalent Cu sites in a commensurate magnetic superstructure should have different hyperfine

Fig. 1. (A) The schematic structure of $SrCu_2(BO_3)_2$ viewed along the c axis. The box shows a unit cell projected on the ab plane. The structure consists of a stack of alternating Cu-B-O magnetic layers and nonmagnetic Sr layers. See (9) for details. **(B)** The Shastry-Sutherland spin model with the intradimer exchange J and the interdimer exchange J', which is topologically equivalent to the Cu network within a layer of $SrCu_2(BO_3)_2$. **(C and D)** Proposed configurations of triplets for the 1/8 magnetization plateau phase (21). Solid circles denote the triplet dimers; numbers distinguish inequivalent Cu sites.

Fig. 2. Cu NMR spectra (black dots) at 35 mK obtained by using a 20-MW resistive magnet at the Grenoble High Magnetic Field Laboratory with a dilution refrigerator. The integrated intensity of Cu spin-echo signal is plotted at discrete frequencies. The inset shows the spectrum at $H_0 = 26$ T. The line is a fit to Eq. 2 (see text). The arrows indicate the peak positions of the fitting. The main panel shows the spectrum at $H_0 = 27.6$ T. The red line is a fit by the sum of contribution from 11 distinct sites, each of which is represented by Eq. 2. The parameter values are listed in table S1. The arrows indicate the resonance frequencies for $H_n = 0$. The strong signal in the range 371 to 379 MHz comes from ^{11}B nuclei; the peak at 125.6 MHz is due to ^{10}B nuclei. The sensitivity of the NMR spectrometer was calibrated using ^{11}B signal at 2 K at several frequencies. Because of unavoidable local variation of the sensitivity, the accuracy of the intensity (vertical) scale is estimated to be typically ±20%.
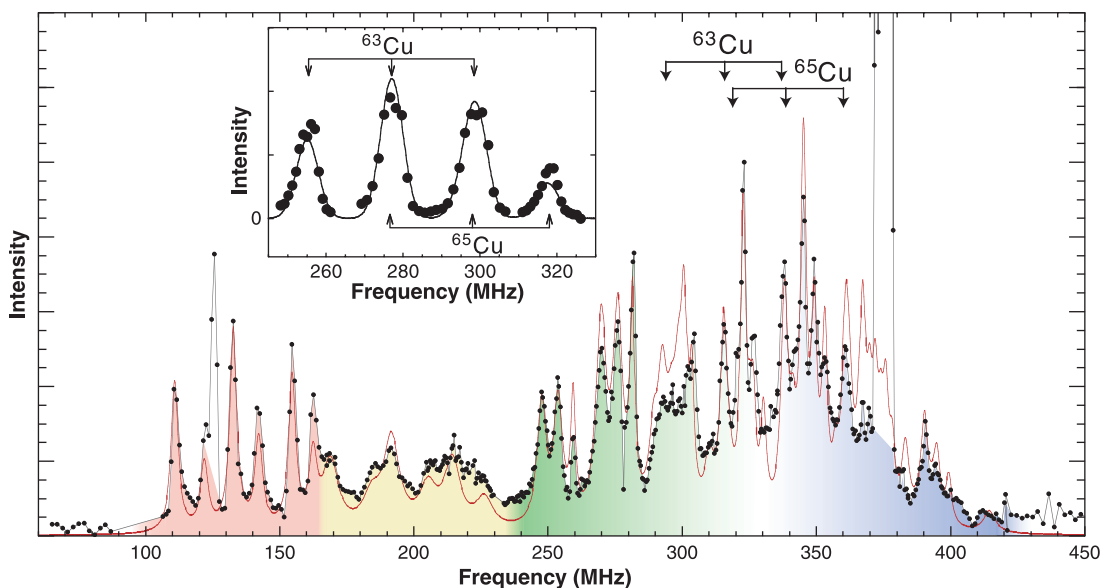
fields that manifest as distinct NMR lines. Therefore, we performed NMR measurements on a single crystal of $SrCu_2(BO_3)_2$ grown by the traveling solvent–floating zone method (25) in a magnetic field up to 28 T applied along the c axis at 35 mK. This covers the first "1/8" magnetization plateau, which has been observed (11) in the field range 27 to 28.5 T.

We show in Fig. 2 the Cu NMR spectra in a field of 26 T (inset) and 27.6 T (main panel). A single Cu site gives six NMR lines at the following frequencies (26),

$$f(\alpha, m) = {}^{\alpha}\gamma[(1+K)H_0 + H_n] + {}^{\alpha}\nu_c(m - 1/2) \quad (2)$$

The first term is the Zeeman frequency due to the external field H_0 corrected for the orbital shift $K = 1.69\%$ (12) and the hyperfine field H_n; ${}^{\alpha}\gamma$ ($\alpha = 63$ or 65) is the known gyromagnetic ratio of either ${}^{63}Cu$ or ${}^{65}Cu$ nuclei. In general, the spin polarizations, both on the same site and on the neighboring sites contribute to H_n. Here we assume only the dominant on-site coupling, $H_n = A_c g_c \langle S_z \rangle$, where $\langle S_z \rangle$ is the time-averaged local magnetization. The coupling constant and the g value were previously determined as $A_c = -23.8$ T/μ_B and $g_c = 2.28$ (12, 13). The second term represents the quadrupolar shift for spin 3/2 nuclei, where $m = 3/2$, 1/2, or $-1/2$ distinguishes three transitions ($I_z = m \rightarrow m - 1$) and ${}^{63}\nu_c = 22.1$ MHz, ${}^{65}\nu_c = 20.5$ MHz as previously determined (12). The Cu NMR spectrum at 26 T can be well fitted by Eq. 2 with a Gaussian distribution of H_n peaked at

−1.79 T with a full width at half maximum (FWHM) of 0.59 T, demonstrating that the system at 26 T is in the uniform phase ($\langle S_z \rangle = 0.033$) where triplets are itinerant.

At a field of 27.6 T, a drastic change of the spectrum was observed with the appearance of many sharp peaks distributed over a wide frequency range, indicative of a commensurate magnetic order with a large unit cell. This is the first clear evidence for a magnetic superlattice in the 1/8 plateau phase with broken translational symmetry. Although the spectrum appears complicated, some important features are immediately recognized. The sharp six peaks at low frequencies, shown by the red zone in Fig. 2, have the intensity approximately 1/8 of the entire spectrum and their positions are given by Eq. 2 with $\langle S_z \rangle = 0.30$. Likewise, the broad lines in the yellow zone in Fig. 2 can be ascribed to a single site with 1/8 population and $\langle S_z \rangle = 0.20$. If the triplets were confined on a single dimer, 1/8 of the Cu sites would have $\langle S_z \rangle = 0.50$ and $\langle S_z \rangle = 0$ for the rest. Therefore, the magnetization must be spread over several sites within the magnetic unit cell. We tried to fit the entire spectrum by progressively adding a new set of lines given by Eq. 2 with a Lorentzian distribution of H_n until all the peaks and the overall shape were reproduced. We found that at least 11 distinct Cu sites had to be included. The population of each site can be chosen to be an integral multiple of 1/16, which is compatible with a magnetic unit cell containing 16 spins. A successful fit is shown by the red line in Fig. 2,

and the corresponding parameters are listed in table S1. The histogram of the peak values of H_n is shown in the middle panel of Fig. 3B. Several sites have positive H_n (blue zone in Fig. 2), implying (through a negative hyperfine coupling) that spins are polarized opposite to the magnetic field direction. Thus, the magnetization oscillates within the unit cell. We confirmed that the average of H_n over all the sites give the spatial average of $\langle S_z \rangle$ to be 0.063, exactly 1/8 of the saturation.

Let us examine whether our results are compatible with the Shastry-Sutherland model. In the simplest theoretical approach, interactions between two triplet dimers are calculated by a perturbation in J'/J (19–21). Two different configurations (Fig. 1, C and D) have been proposed for the 1/8 plateau (21). Here, each triplet is completely localized on one dimer, the result of an oversimplification of this approach. The real magnetization of the Shastry-Sutherland model spreads over all the sites, as explained below. The number of inequivalent Cu sites, however, does not depend on such details of the magnetization profile and can be determined only from symmetry considerations. For the square cell, there are six distinct Cu sites, as shown in Fig. 1C. The number of Cu sites may increase depending on how the layers stack along the c axis, however, only up to eight, which is clearly not sufficient to reproduce all the observed peaks. On the other hand, the rhomboid cell has eight Cu sites for a single layer (Fig. 1D) and the stacking of layers may increase the number up to 16, although all the sites may not be resolved experimentally. Therefore, we may expect that only the rhomboid cell is compatible with the experiments.

To go beyond these qualitative considerations and check whether the Shastry-Sutherland model can indeed reproduce the peculiar spin texture revealed by NMR, with positive and negative magnetizations, we must solve the original spin Hamiltonian of Eq. 1 for a finite-size lattice. There is a subtlety, though. If the ground state breaks the translational symmetry, it is expected to be eightfold degenerate for an infinite system and the ground-state magnetization is not well defined. In the actual compound, a unique ground state would be selected by pinning from impurities or from a lattice distortion. In our finite-size calculation, although periodic boundary condition partially lifts the eightfold degeneracy, some mechanism still must be added to the model to enable selection of one of the ground states (27). Because the pronounced softening of the sound velocity observed at the edges of the magnetization plateaus (16) suggests that a lattice distortion indeed occurs in $SrCu_2(BO_3)_2$, we decided to include an adiabatic spin-phonon coupling (28),
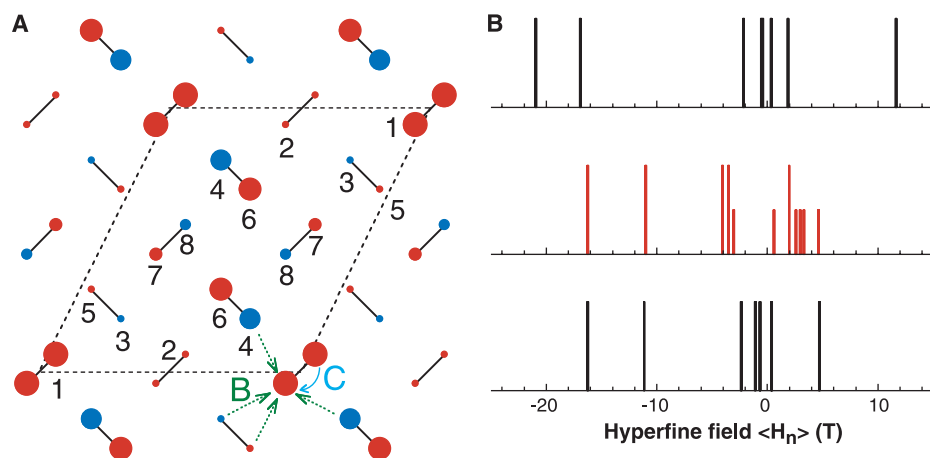

Fig. 3. (A) Magnetization profile obtained as described in the text. Red circles indicate positive $\langle S_z \rangle$, blue circles indicate negative $\langle S_z \rangle$, and circle size represents the magnitude of $\langle S_z \rangle$. The calculated values for $\langle S_z \rangle$ are 0.386 (site 1), 0.010 (site 2), −0.0063 (site 3), −0.215 (site 4), 0.0073 (site 5), 0.312 (site 6), 0.040 (site 7), and −0.035 (site 8). **(B)** Histogram of the hyperfine field $\langle H_n \rangle$. The middle panel (red) shows the results of the fitting of the NMR spectrum (Fig. 2, red line) (table S1). Long lines indicate that the population of the site is 1/8; short lines indicate that the population of the site is 1/16. The top panel is obtained from the theoretical magnetization profile in (A) assuming only the on-site hyperfine coupling $A = A_c = -23.8$ T/μ_B as described in the text. Generally there are also transferred hyperfine couplings to neighboring spins, denoted B and C in (A), but these are much smaller than the on-site coupling and are difficult to estimate. The bottom panel is obtained from the theoretical profile in (A) assuming $B = -1.04$, $C = -2.45$ T/μ_B. [The previous low-field data (12) put the constraint $A = A_c - 4B - C$.] The improved agreement with experiments, however, is only indicative.

$$H = \sum_{(n.n.)} J\left(1-\alpha\frac{\delta d_{ij}}{d_{ij}^0}\right)\mathbf{S}_i \cdot \mathbf{S}_j + \sum_{(n.n.n.)} J'\left(1-\alpha'\frac{\delta d_{ij}}{d_{ij}^0}\right)\mathbf{S}_i \cdot \mathbf{S}_j$$

$$+ \frac{K}{2}\sum_{(n.n.)}\left(\frac{\|\delta\mathbf{r}_i - \delta\mathbf{r}_j\|}{d_{ij}^0}\right) + \frac{K'}{2}\sum_{(n.n.n.)}\left(\frac{\|\delta\mathbf{r}_i - \delta\mathbf{r}_j\|}{d_{ij}^0}\right)^2 \quad (3)$$

parameterized by the spin-phonon coupling constants α and α' and the elastic constants K and K'. The exchange constants now depend on the deviation of the interatomic distance δd_{ij} from the value d_{ij}^0 in the uniform phase. The atomic displacements $\delta\mathbf{r}_i$ are free to adjust to give the best compromise between the increase of elastic energy and the gain in magnetic energy. The Hamiltonian of Eq. 3 was solved by exact diagonalization of a 16-spin (eight-dimer) cluster, using the Lanczos algorithm imposing periodic boundary conditions compatible with the rhomboid cell and a total magnetization of 1/8, and by minimizing the energy with respect to $\delta\mathbf{r}_i$. Similar calculations have been performed in the context of spin-Peierls systems such as $CuGeO_3$ (29).

The results of Fig. 3A were obtained assuming typical values $\alpha = \alpha' = 7$ and $K = K' = 20,000$ K for oxides (27) and using well-accepted values for the exchange constants, $J = 85$ K and $J' = 54$ K (30). The magnetization profile extends over the entire unit cell, with one strongly polarized dimer surrounded by decaying oscillation of magnetization. Similar structure has also been observed around impurities in quantum spin chains (31, 32) and two-dimensional superconducting cuprates (33). It is analogous to the Friedel oscillation near impurities in metals. The calculated profile captures the essential feature of the experimental results (Fig. 3B), providing further support for the rhomboid cell. Note that the coupling to phonons

is required merely to select one of the degenerate ground states and is not necessary to obtain a plateau. The magnetization pattern depends only weakly on the value of the spin-phonon coupling (fig. S1); therefore, the qualitative feature mentioned above is expected to be an intrinsic aspect of the magnetic system. Note also that the displacements we obtain (table S2) are very small—less than 1%, which would not be possible to detect experimentally in a magnetic field of 27 T with facilities currently available.
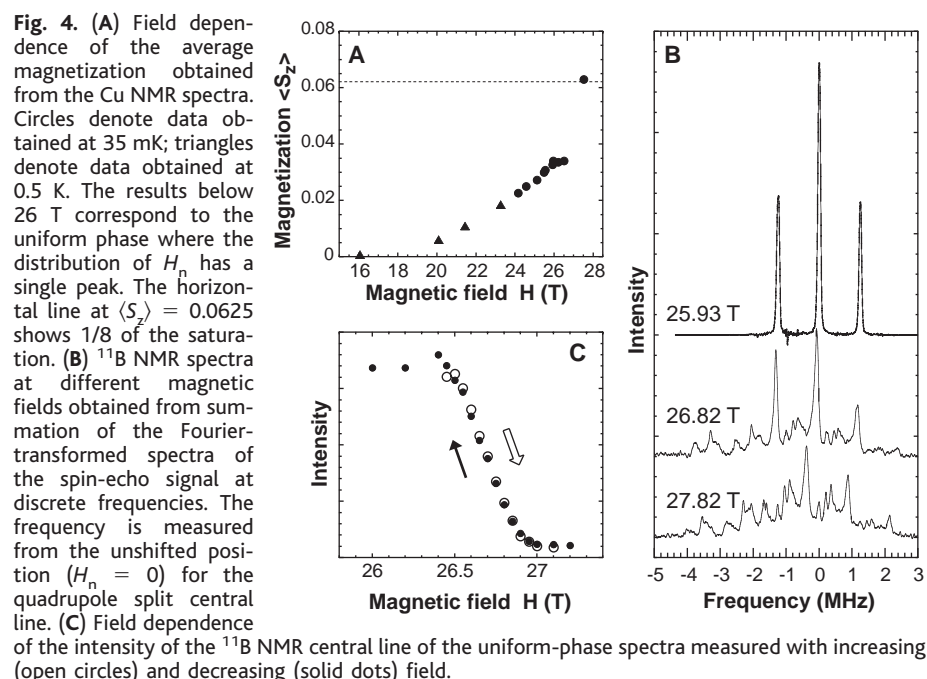
We now discuss the nature of the phase transition into the 1/8 plateau state. The field dependence of the magnetization obtained from the Cu NMR spectra (Fig. 4A) shows a nearly discontinuous jump upon entering the 1/8 phase. The vicinity of the phase boundary was studied by the ^{11}B NMR spectra obtained at 35 mK (Fig. 4B). The ^{11}B spectra are much narrower than the Cu spectra and are easier to obtain. In agreement with the Cu NMR results, the spectrum at 25.93 T with three sharp peaks split by the quadrupolar interaction indicates a uniform magnetization, whereas the rich structure of the spectrum at 27.82 T points to a magnetic superlattice. If the transition were second order and there were no disorder, we would expect that the spectral shape changes continuously with the field. This is, however, not the case: The spectrum at 26.82 T is a superposition of two types of spectra, each of which is identical to the spectrum at 25.93 T or 27.82 T. Thus, the two phases coexist at this field. The volume fraction of the uniform phase, given by the intensity of the sharp central peak, continuously changes in the field range 26.4 to 27 T without hysteresis (Fig. 4C). Such behavior

can be explained if the transition is first order but broadened by some disorder in the sample, which enables nucleation of the magnetic superlattice with small domain size. Interestingly enough, this is consistent with the Landau-Lifshitz theory, according to which the transition is expected to be first order when the ordering wave vector does not lie on a high-symmetry point; the ordering wave vector $k = (\pi/a, \pi/2a)$ for the rhomboid cell is not a high-symmetry point (27).

Quantum melting of various ordered structures—for example, vortex lattices in superconductors and charge or orbital order in perovskite transition metal oxides—has been attracting increasing attention. In many cases, the phase transition is controlled by chemical doping, which also introduces disorder and increases complexity. Here we have a clean system with an exotic ordered structure, in which the phase transition can be tuned by a magnetic field. As the temperature is increased, we also expect a melting transition, which should be discontinuous for the same reasons discussed for the field-induced zero-temperature transition (27). This remains to be studied; at present we only know that the ^{11}B NMR spectrum at 1.5 K shows no signature of superstructure.

References and Notes

1. E. Abrahams, G. Kotliar, *Science* **274**, 1853 (1996).
2. Special issue on Correlated Electron Systems, *Science* **288**, 461 (2000).
3. E. Dagotto, T. M. Rice, *Science* **271**, 618 (1996).
4. M. Oshikawa, M. Yamanaka, I. Affleck, *Phys. Rev. Lett.* **78**, 1984 (1997).
5. K. Totsuka, *Phys. Rev. B* **57**, 3454 (1998).
6. Y. Narumi *et al.*, *Physica B* **246–247**, 509 (1998).
7. W. Shiramura *et al.*, *J. Phys. Soc. Jpn.* **67**, 1548 (1998).
8. M. Oshikawa, *Phys. Rev. Lett.* **84**, 1535 (2000).
9. R. W. Smith, D. A. Keszler, *J. Solid State Chem.* **93**, 430 (1991).
10. H. Kageyama *et al.*, *Phys. Rev. Lett.* **82**, 3168 (1999).
11. K. Onizuka *et al.*, *J. Phys. Soc. Jpn.* **69**, 1016 (2000).
12. K. Kodama *et al.*, *J. Phys. Condens. Matter* **14**, L319 (2002).
13. H. Nojiri, H. Kageyama, K. Onizuka, Y. Ueda, M. Motokawa, *J. Phys. Soc. Jpn.* **68**, 2906 (1999).
14. H. Kageyama *et al.*, *Phys. Rev. Lett.* **84**, 5876 (2000).
15. O. Cépas *et al.*, *Phys. Rev. Lett.* **87**, 167205 (2001).
16. B. Wolf *et al.*, *Phys. Rev. Lett.* **86**, 4847 (2001).
17. M. Albrecht, F. Mila, *Eur. Phys. J. B* **34**, 145 (1996).
18. S. Miyahara, K. Ueda, *Phys. Rev. Lett.* **82**, 3701 (1999).
19. T. Momoi, K. Totsuka, *Phys. Rev. B* **61**, 3231 (2000).
20. _____, *Phys. Rev. B* **62**, 15067 (2000).
21. S. Miyahara, K. Ueda, *Phys. Rev. B* **61**, 3417 (2000).
22. A. Koga, N. Kawakami, *Phys. Rev. Lett.* **84**, 4461 (2000).
23. G. Misguich, Th. Jolicoeur, S. M. Girvin, *Phys. Rev. Lett.* **87**, 097203 (2001).
24. B. S. Shastry, B. Sutherland, *Physica B* **108**, 1069 (1981).
25. H. Kageyama, K. Onizuka, T. Yamauchi, Y. Ueda, *J. Cryst. Growth* **206**, 65 (1999).
26. A. Abragam, *Principles of Nuclear Magnetism* (Clarendon, Oxford, UK, 1961).
27. See supporting data on *Science* Online.
28. An alternative way of selecting a unique ground state is to add a symmetry-breaking external field, as is often done in the simpler case of spin-Peierls transition. In our case, however, this would bias the results because we do not know a priori the magnetization pattern.

Fig. 4. (A) Field dependence of the average magnetization obtained from the Cu NMR spectra. Circles denote data obtained at 35 mK; triangles denote data obtained at 0.5 K. The results below 26 T correspond to the uniform phase where the distribution of H_n has a single peak. The horizontal line at $\langle S_z \rangle = 0.0625$ shows 1/8 of the saturation. **(B)** ^{11}B NMR spectra at different magnetic fields obtained from summation of the Fourier-transformed spectra of the spin-echo signal at discrete frequencies. The frequency is measured from the unshifted position ($H_n = 0$) for the quadrupole split central line. **(C)** Field dependence of the intensity of the ^{11}B NMR central line of the uniform-phase spectra measured with increasing (open circles) and decreasing (solid dots) field.

29. A. Dobry, J. A. Riera, *Phys. Rev. B* **56**, R2912 (1997).
30. S. Miyahara, K. Ueda, *J. Phys. Soc. Jpn.* **69** (suppl. B), 72 (2000).
31. M. Takigawa, N. Motoyama, H. Eisaki, S. Uchida, *Phys. Rev. B* **55**, 14129 (1997).
32. F. Tedoldi, R. Santachiara, M. Horvatić, *Phys. Rev. Lett.* **83**, 412 (1999).
33. M.-H. Julien *et al.*, *Phys. Rev. Lett.* **84**, 3422 (2000).
34. We thank J. L. Gavilano and P. Van der Linden for help

Stimulated Raman Scattering in Hydrogen-Filled Hollow-Core Photonic Crystal Fiber

F. Benabid,* J. C. Knight, G. Antonopoulos, P. St. J. Russell

We report on stimulated Raman scattering in an approximately 1-meter-long hollow-core photonic crystal fiber filled with hydrogen gas under pressure. Light was guided and confined in the 15-micrometer-diameter hollow core by a two-dimensional photonic bandgap. Using a pulsed laser source (pulse duration, 6 nanoseconds; wavelength, 532 nanometers), the threshold for Stokes (longer wavelength) generation was observed at pulse energies as low as 800 ± 200 nanojoules, followed by a coherent anti-Stokes (shorter wavelength) generation threshold at 3.4 ± 0.7 microjoules. The pump-to-Stokes conversion efficiency was $30 \pm 3\%$ at a pulse energy of only 4.5 microjoules. These energies are almost two orders of magnitude lower than any other reported energy, moving gas-based nonlinear optics to previously inaccessible parameter regimes of high intensity and long interaction length.

A long-standing challenge in nonlinear optics is the maximization of nonlinear interactions between laser light and low-density media such as gases. The requirements for efficient nonlinear processes are high intensity at low power, a long interaction length, and a good-quality transverse beam profile. A conceptual structure capable of delivering all these requirements simultaneously is a perfectly guiding, hollow-core waveguide supporting a single transverse mode with low attenuation losses. Theoretically, this could be realized by using a perfect metal. However, the attenuation in real metals at optical frequencies is too high. We report here the use of a hollow-core photonic crystal fiber (HC-PCF) (*1*) to achieve efficient stimulated Raman scattering (SRS) in hydrogen gas.

Unlike in hollow fiber capillaries, light is trapped in an HC-PCF by a two-dimensional photonic band gap (PBG) created by a "photonic crystal" of microcapillaries filling the region around the hollow core (*2*). Although theory shows that light can be guided in a single transverse mode without loss, typical current HC-PCFs display attenuation losses on the order 1 dB/m. Such low attenuation, allied with a very small core area ($\sim$100 μm^2), make HC-PCF a promising "host" for

Raman active gases, offering ultralong interaction lengths while keeping the laser beam tightly confined in a single mode.

A number of conventional approaches have been used to enhance SRS in gases. These include focusing a laser beam into the gas with suitable optics, using a $\sim$200-μm-bore fiber capillary to confine the gas and provide some degree of guidance for the light (*3*), and employing a gas-filled high-finesse Fabry-Pérot cavity to increase the interaction length (*4*). It is instructive to compare these with HC-PCF, using the figure of merit $f_{om} = L_{int}\lambda/A_{eff}$, where L_{int} is the effective constant-intensity interaction length and A_{eff} is the effective cross-sectional area. Focusing a la-

ser beam with conventional optics produces approximately constant high intensity over a distance equal to twice the Rayleigh length $z_R = \pi w_o^2/\lambda$, where w_o is half the beam width at the focus and λ is the vacuum wavelength; in this case, $f_{om} \sim 16$. In a fiber capillary, the figure of merit takes the form

$$f_{om} = \frac{6.8a(n^2-1)}{\lambda\pi\sqrt{n^2+1}} \qquad (1)$$

where n is the refractive index of the glass, and we used the results reported in (*5*). This increases in a linear fashion with bore radius a, indicating that small-core capillaries make poor waveguides. For a hollow-core PCF, the figure of merit takes the form

$$f_{om} = \frac{\lambda}{\pi a^2 \alpha} \qquad (2)$$

where α is the exponential attenuation rate of the intensity. These three expressions are plotted (Fig. 1) for silica glass ($n = 1.46$) at a wavelength of 532 nm.

The HC-PCF has clear advantages, particularly when the bore is small. At a diameter of 10 μm, for example, a free-space beam is preferable to a capillary, whereas an HC-PCF with a loss of 0.3 dB/m is almost 10,000 times more effective. Improvements in all sorts of nonlinear laser-gas interactions should become possible, such as ultralow-threshold SRS in gases.

SRS is a two-photon linear inelastic light-scattering process, in which an incoming photon interacts with a coherently excited state of the system (in our case, one of the vibrations of a hydrogen molecule). As a
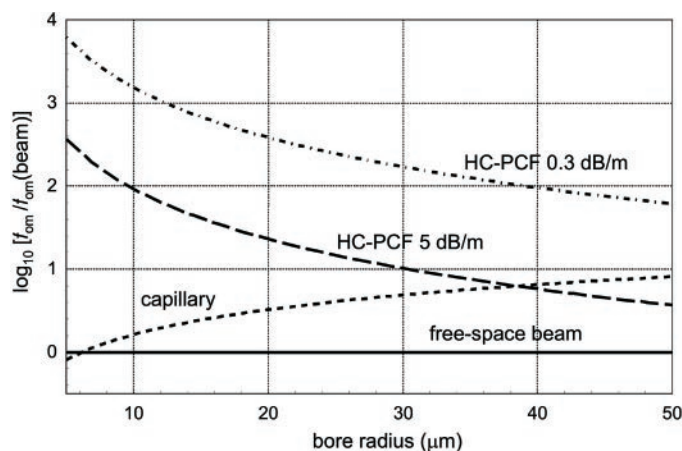
Optoelectronics Group, Department of Physics, University of Bath, Claverton Down, Bath BA2 7AY, UK.

*To whom correspondence should be addressed. E-mail: pysab@bath.ac.uk

Fig. 1. Figures of merit for a hollow capillary and two HC-PCFs, relative to the value for a free-space beam. At a bore radius of 5 μm, the HC-PCF is almost 10,000 times better.